

Thin-film superconducting NbTi microwave resonators for cryogenic thermometry

A. Chatel,¹ R. Russo,¹ L. Mazzone,¹ Q. Boinay,¹ R. Farsi,¹ J. Brugger,¹ G. Boero,^{1,2} and H. Furci¹

¹*Microsystems Laboratory, École Polytechnique Fédérale de Lausanne (EPFL), 1015 Lausanne, Switzerland*

²*Center for Quantum Science and Engineering, École Polytechnique Fédérale de Lausanne (EPFL), 1015 Lausanne, Switzerland*

(*Electronic mail: andre.chatel@epfl.ch)

(Dated: 27 March 2025)

Superconducting microwave resonators have recently gained a primary importance in the development of cryogenic applications, such as circuit quantum electrodynamics, electron spin resonance spectroscopy and particles detection for high-energy physics and astrophysics. In this work, we investigate the influence of the film thickness on the temperature response of microfabricated Nb₅₀Ti₅₀ superconducting resonators. S-shaped split ring resonators (S-SRRs), 20 nm to 150 nm thick, are designed to be electromagnetically coupled with standard Cu coplanar waveguides (CPWs) and their microwave properties are characterized at temperatures below 10 K. The combined contributions of the kinetic inductance $L_K(T)$ increase and the decreasing loaded quality factor Q_L induce an optimum condition on the temperature sensitivity and resolution of the resonators, for thinner films. A noise equivalent temperature (NET) as low as $0.5 \mu\text{K}/\text{Hz}^{1/2}$, at 1 Hz, is reported for 100 nm thick resonators at 4.2 K. We also assess the possibility of implementing a multiplexed frequency readout, allowing for the simultaneous temperature tracking of several sensors along a single CPW. Such results demonstrate the possibility to perform a distributed cryogenic temperature monitoring, with a sub- μK resolution. In such a perspective, superconducting S-SRRs, eventually benefiting from an even higher $L_K(T)$, might be exploited to accurately monitor the on-chip temperature of devices operating in cryogenic conditions.

In the last decades, microwave systems operating at temperatures well below 90 K have experienced a growing interest from the scientific community. In this framework, superconducting thin-films have paved the way for novel techniques and devices relying on low temperature quantum phenomena. Among different technologies, superconducting resonators have proven to be key elements for the design of microwave kinetic inductance detectors (MKIDs)^{1–5}, circuit quantum electrodynamics architectures (QED)^{6–8} and qubits^{9–12}, ultra-low noise quantum parametric amplifiers^{13–15} and detectors for electron spin resonance (ESR) spectroscopy^{16–19}. Dealing with all the aforementioned applications, the accurate monitoring of the on-chip temperature is crucial for ensuring the correct functioning of the device. Commercially-available cryogenic thermometers, as CERNOX^{®20} or RuO₂²¹ thin-film thermistors, generally show temperature resolutions around $100 \mu\text{K}$, below 10 K.^{22,23} Superconducting materials have also been investigated as alternatives to perform cryogenic thermometry, with DC CMOS-compatible devices²⁴ and microwave resonators²⁵ having reported temperature resolutions, respectively, around $3 \text{ mK}/\text{Hz}^{1/2}$ and $75 \mu\text{K}/\text{Hz}^{1/2}$, for $T < 1 \text{ K}$. More specifically, the superconducting properties in the microwave range can be exploited to realize resonators able to correlate changes in the cryogenic temperature to frequency shifts^{25–27}, with the potential of performing a temperature readout in parallel with the operation of the chip. The possibility of exploiting high quality factors, larger than 10^4 , the absence of additional interconnections and the ease of performing an accurate on-chip temperature monitoring make superconducting microwave resonators an attractive alternative to more conventional cryo-thermistors.²⁵

In this work, we report on the dependence of the temperature sensitivity and resolution of superconducting microres-

onators on the superconducting film thickness. The aim of this study is to provide guidelines for the optimization of the performances of cryogenic thermometers based on the variation of the thin-film kinetic inductance. As a matter of fact, our findings demonstrate that, even though thinner films increase the temperature sensitivity of the resonators, as depending on the increasing $L_K(T)$, an excessive thinning of the superconducting film also entails a drastic reduction of the quality factor, inducing an increase in the minimum detectable temperature variations. In such a sense, a trade-off between temperature sensitivity and resolution has to be carefully evaluated in the design phase, in order to determine an optimal film thickness.

The kinetic inductance $L_K(T)$ of superconducting materials is an electronic-transport parameter originating from the low inertia of Cooper pairs, whose density $n_S(T)$ significantly decreases for temperatures approaching the superconducting-to-normal critical transition.^{28–31} In particular, considering a thin-film superconducting resonator, with length l , width w and normal state surface resistance $R_\square(T_C)$, it is possible to model the temperature influence on its resonance frequency, close to the transition temperature T_C and in the low frequency regime $\hbar\omega \ll k_B T$, as^{31,32}

$$f_{\text{res}}(T) = \frac{1}{2\pi\sqrt{(L_G + L_K(T))C_G}} \quad (1a)$$

$$L_K(T) = \frac{\hbar R_\square(T_C)}{\pi\Delta(T)} \frac{1}{\tanh\left(\frac{\Delta(T)}{2k_B T}\right)} \left(\frac{l}{w}\right) \quad (1b)$$

where $\Delta(T) \simeq 1.74\Delta(0)\sqrt{1-T/T_C}$ is the superconducting energy gap and $\Delta(0) = 1.76k_B T_C$, while L_G and C_G stand, re-

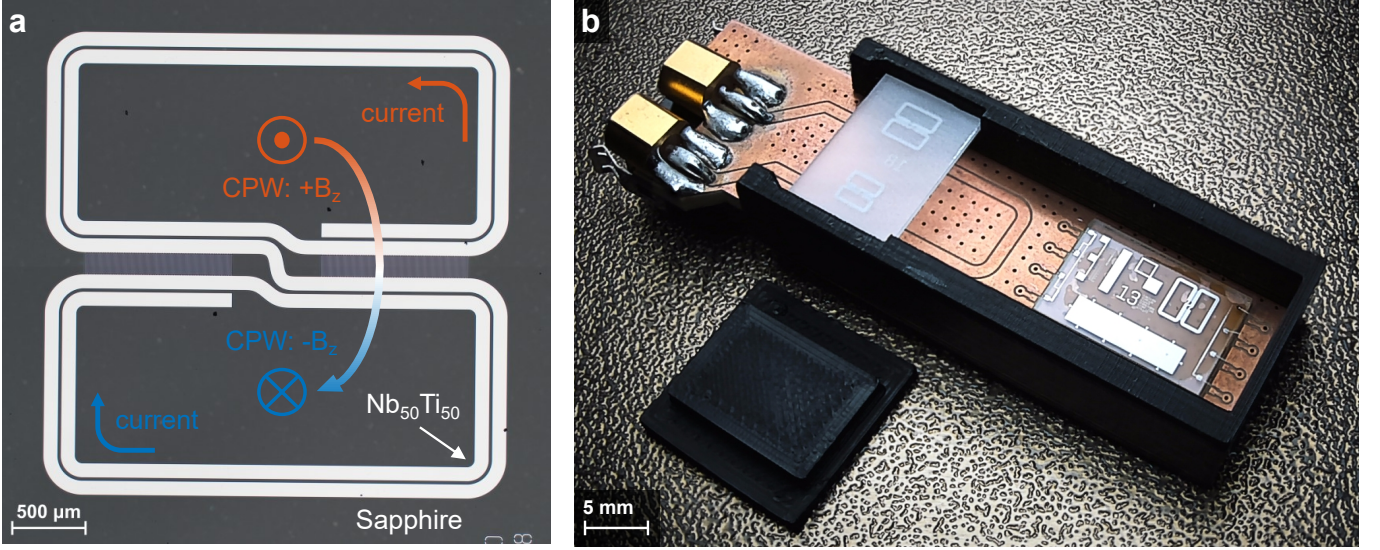


FIG. 1. Description of the S-SRR chips. a) Optical microscope picture of the 1.1 GHz resonator under test. The coloured arrow represents the direction of the antisymmetric B-field of a GCPW underneath. b) PCB exploited for the characterization of the resonators in cryogenic environments. The separation distance between the chip and the Cu GCPW is set by the black PLA support; a plastic lid (bottom-left) and Kapton-tape are exploited to keep the suspended chip in position. A chip containing 4-wires structures, for the $\text{Nb}_{50}\text{Ti}_{50}$ films cryogenic DC characterization, is wire-bonded at the bottom-right of the PCB.

spectively, for the geometric inductance and capacitance of the resonator.

In order to study the influence of the film thickness on the temperature response of superconducting resonators, several $\text{Nb}_{50}\text{Ti}_{50}$ films, with the thickness ranging from 20 nm to 150 nm, are DC sputtered, at room temperature, on C-plane sapphire wafers. The choice for $\text{Nb}_{50}\text{Ti}_{50}$ resides on its transition parameters, showing critical DC field values as high as 15 T^{33–35} and microwave ones larger than 350 mT³⁶, reducing the influence of magnetic field fluctuations. Moreover, a bulk critical temperature up to 10 K^{33,37–39} makes this material suitable for temperature ranges commonly achieved by cryogenic applications based on liquid He (LHe) cooling. Sapphire is exploited as substrate material because of its exceptional microwave properties in ultra-cold environments,^{40–42} as, for instance, a high dielectric constant ϵ_r around 10 and an extremely low loss factor ϵ'' , down to 10^{-9} . A lower bound for the surface kinetic inductance of such films is estimated through the $L_K(T)$ at $T = 0$ K,^{31,43} with the value of the different normal state surface resistances measured just above the critical transition by means of a 4-wires patterned structure. In Table I we report the estimated surface kinetic inductances. A maximum of 11 pH/□ is obtained for the 24 nm thick film. The use of nitride-based superconducting thin-films, such as NbN and NbTiN^{43–45} could lead to larger $L_K(0)$ and, eventually, to better sensitivity and resolution when used for cryogenic thermometry.

Among different planar geometries, S-shaped split ring resonators (S-SRRs) have been reported as ideal candidates for providing an optimal electromagnetic coupling with microwave coplanar waveguides (CPWs),^{46–48} due to the possibility of exciting two counter-twisted inductive loops with antisymmetric magnetic field configurations [see Fig. 1(a)]. In

TABLE I. $\text{Nb}_{50}\text{Ti}_{50}$ critical surface resistance, 0 K kinetic inductance, critical temperature, geometric inductance and capacitance of the resonators, for different thin-film thicknesses.

t (nm)	$R_{\square}(T_C)^a$ (Ω/\square)	$L_K(0)$ (pH/□)	T_C^b (K)	L_G^b (nH)	C_G^b (fF)
24	51	11	6.2	48	440
57	17	3.2	7.7	35	560
105	8.7	1.5	8.1	29	660
147	5.7	0.99	8.1	27	710

^a Extracted from a 4-wires V/I measurement.

^b Fitting parameters from the $L_K(T)$ -based model presented in Eq. 1.

such a perspective, $\text{Nb}_{50}\text{Ti}_{50}$ S-SRRs are patterned on 650 μm thick sapphire wafers, recurring to a combination of direct laser writing (DLW) photolithography and SF_6/CHF_3 -based plasma etching. More details about the micro-fabrication of the thin-film resonators are reported in the [supplementary material](#). The S-SRR geometry consists of 2-turns top and bottom loops (3.20 mm \times 1.52 mm). The inductive stripe shows length and width values, respectively, equal to 37 mm and 100 μm . An inter-line gap of 20 μm separates each turn, while two interdigitated capacitors (IDCs), made up of 340 fingers (length: 148 μm , width: 4 μm , gap: 2 μm), are located between the two loops. Such additional capacitors are intended to maintain the compactness of the device, while lowering down its resonance frequency and limiting, therefore, the degradation of the quality factor induced by the $\propto f^2$ increase of the superconducting surface resistance.^{30,31,49}

COMSOL Multiphysics[®] finite element method (FEM)

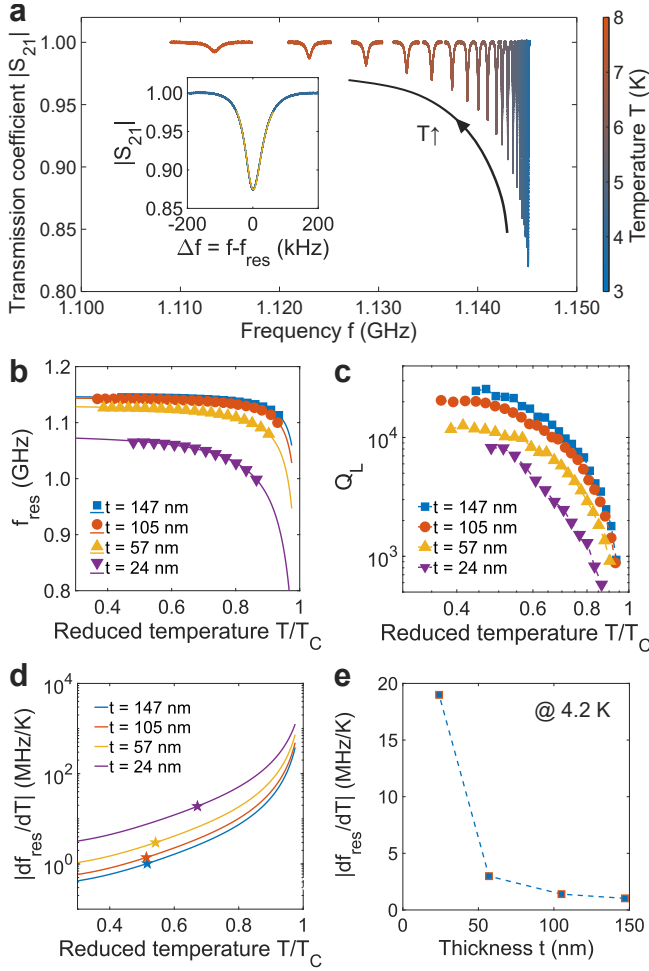


FIG. 2. Temperature response of the S-SRRs for different film thicknesses. a) Temperature-induced resonance frequency shifts for the 147 nm thick sample. The inset shows the $|S_{21}|$ resonance at 4.2 K, with the blue line representing the measured data, while the yellow one stands for the fit to a skewed-Lorentzian curve ($f_{res} = 1.1442$ GHz and $Q_L = 1.75 \times 10^4$). b) Resonance frequency shifts for the different film thicknesses: the solid line represents the $f_{res}(T)$ model, fitted to the data points. c) Temperature evolution of the loaded Q-factor. d) Temperature evolution of the S-SRRs sensitivity, estimated as the derivative of the $f_{res}(T)$ fitting model. The single points refer to the value at 4.2 K. e) Temperature sensitivity of the different S-SRRs, evaluated at 4.2 K.

simulations are performed to optimize the S-SRR geometry for coupling inductively to a standard Cu grounded CPW (GCPW) and resonating approximately around 1.1 GHz (see the [supplementary material](#)). The chips are coupled face-down to a 50Ω GCPW by means of a 3D-printed polylactide (PLA) support, allowing to precisely place the S-SRRs with the two inductive loops centered on top of the transmission line gaps, as shown in [Fig. 1\(b\)](#). In such a configuration, the critical coupling parameter turns out to be the distance d_{cpl} between the chip and the printed circuit board (PCB). In order to provide an optimal coupling, several tests are carried out in liquid He on the 147 nm thick resonator, increasing d_{cpl} from 1.5 mm up to 5.0 mm: as reported in the [supplementary](#)

[material](#), a distance value of 2.5 mm is chosen, as it allows to excite the devices with approximately 50% of the transmitted power, still preserving loaded quality factor Q_L values larger than 10^4 .

In order to investigate the temperature response of the resonators for different thicknesses, the S-SRRs are cooled down, in zero-field conditions, to temperatures as low as 3 K, by means of the variable temperature insert (VTI) of a dry superconducting cryomagnet. A 2-port vector network analyzer (VNA), directly connected in transmission to the PCB, is exploited to excite each device with a power of -18 dBm, allowing to record the S-parameters of the system. The temperature monitoring and control is achieved through the use of two CERNOX[®] thermometers and two heaters (see the [supplementary material](#)). In [Fig. 2\(a\)](#) we report the typical S_{21} spectral response below T_C . The effect of the microwave lines is eliminated by acquiring frequency scans at a temperature slightly above the superconducting transition and subtracting such backgrounds, in the complex domain, to the corresponding resonance signals.^{50,51} The values of the resonance frequency f_{res} and the loaded quality factor Q_L are, then, extracted through a fit to a skewed-Lorentzian curve⁵² (typically $R^2 > 99.9\%$ for $T/T_C < 0.8$). The temperature response of the different S-SRRs is compared in [Fig. 2\(b\)](#), with the data-points being fitted to the $f_{res}(T)$ model from [Eq. 1](#). The resonance frequency of each device decreases as the temperature approaches the critical transition, consistently with the increase of the kinetic inductance term $L_K(T)$.²⁹ Moreover, an overall shift towards lower frequencies for $f_{res}(0)$ is observed, which can probably be attributed to the increase of the geometric inductance L_G , induced by the smaller cross-section of the thinner films. As described by [Table I](#), the increase in the L_G term is well reflected by the evolution of such fitting parameter, as well as the critical temperature T_C follows the saturation trend reported in literature for thicker films^{29,53}. Additionally, the loaded quality factor Q_L , even though showing values as high as 2.5×10^4 , is found to experience a decrease with respect to the reduction of the S-SRRs thickness, most probably due to the larger microwave resistance of the thinner films [see [Fig. 2\(c\)](#)]. The temperature sensitivity of each resonator is also estimated, by means of the $f_{res}(T)$ analytical model. The result is reported in [Fig. 2\(d-e\)](#) together with the evidence of the higher overall sensitivity for the devices characterized by larger values of kinetic inductance. In particular, an almost 20-fold larger sensitivity value of 19 MHz/K, is achieved, with respect to the 147 nm thick S-SRR, for the 24 nm thick one, at 4.2 K.

The temperature resolution of such superconducting devices is estimated at 4.2 K in a LHe dewar, in order to eliminate all sources of environmental noise related to temperature and remanent magnetic field fluctuations of the VTI chamber. Additionally, a more complex experimental setup, based on a frequency modulation (FM) lock-in detection scheme, is implemented [see [Fig. 3\(a\)](#)]. A microwave signal generator is exploited to excite the S-SRRs with a -20 dBm power, frequency-modulated at 11 kHz with a deviation of ± 5 kHz. The choice of these three values is justified in the [supplementary material](#). The microwave transmitted signal is am-

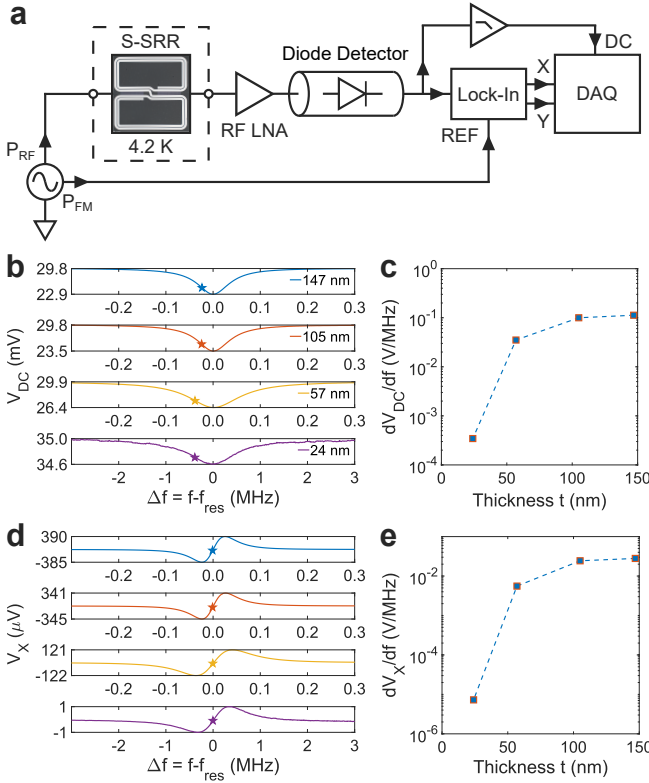


FIG. 3. Frequency response of the S-SRRs for different film thicknesses. a) Experimental setup used to characterize the devices in liquid He at 4.2 K b) DC component of the resonance signal: the single points represent the maximum slope condition. c) Maximum slope of the DC component versus film thickness. d) X-component of the lock-in output signal: the single points represent the maximum slope condition, in this case located at the resonance frequency. The color legend is the same as the one reported for the DC signal graph. e) Maximum slope of the X-component versus film thickness.

plified and converted into a DC value proportional to its amplitude with a microwave diode detector. The different components of the signal are then split, with the DC one further amplified, and the 11 kHz AC one detected by means of a lock-in amplifier, with a 2.5 Hz equivalent noise bandwidth (*i.e.* 100 ms time constant). Finally, both DC, in-phase (X) and quadrature (Y) components are simultaneously acquired by a data acquisition (DAQ) board with a 100 ms integration time (more details are presented in the [supplementary material](#)). Such a characterization setup is preferred to more conventional schemes, relying on VNAs^{25,26,43} and homodyne readout systems^{54,55}, to investigate the possible application of signal modulation techniques for reducing the influence of the instrumentation noise at lower frequencies. In Fig. 3(b-c) we report the frequency response of the DC component of the resonance signal. The dependance of the loaded quality factor Q_L on the film thickness, already observed in the previous variable-temperature experiments, affects the slope of the resonance curves. In particular, when thinning down the Nb₅₀Ti₅₀ film from 147 nm to 24 nm, we observe a reduction of Q_L by a factor of 20 and a reduc-

tion of the slope by a factor of 300 (from 1.1×10^{-1} V/MHz to 3.5×10^{-4} V/MHz). Such a strong reduction of Q_L also impacts the response of the resonators in terms of the signal X component [see Fig. 3(d-e)], where limiting values of 2.8×10^{-2} V/MHz and 7.3×10^{-6} V/MHz define the maximum slope conditions for the thickest and thinnest devices respectively.

The temperature resolution, or noise equivalent temperature (*NET*), expressed in K/Hz^{1/2}, is defined as

$$NET(f_{noise}) = \frac{NSD(f_{noise})}{R} \quad (2a)$$

$$R = \frac{dV}{dT} = \frac{dV}{df} \cdot \frac{df}{dT} \quad (2b)$$

where $NSD(f_{noise})$ is the noise spectral density (in V/Hz^{1/2}), while R is the temperature responsivity of the device (in V/K) as the product between the slope of the sensing signal (*i.e.* either DC or X) and the temperature sensitivity of the resonance frequency. The low-frequency NSDs, below 40 Hz, are extracted by applying the fast Fourier transform (FFT) on a 2 h time monitoring of both the DC and X signals, with 5 ms lock-in and DAQ integration times. Fig. 4(a) shows the *NET* frequency spectrum for the 147 nm thick S-SRR, estimated by means of Eq. 2. The *NET* associated to the DC signal clearly shows a $1/f$ behavior below 10 kHz, which might be associated to the electronic noise coming from the setup instrumentation. In particular, a temperature resolution of about $6 \mu\text{K}/\text{Hz}^{1/2}$ is achieved for such a signal at 1 Hz. The FM transfer of the sensing signal above the $1/f$ corner frequency, minimizes the influence of the instrumentation noise and allows to improve the temperature resolution of the device almost by a factor 10, with a *NET* around $0.7 \mu\text{K}/\text{Hz}^{1/2}$ for the X signal at 1 Hz. The higher temperature sensitivity of thinner devices is counterbalanced by the degradation of the quality factor (*i.e.* curve slope dV/df). As previously discussed, these two effects contribute in originating an optimum condition for the best temperature resolution. Considering the X signal evaluated at 1 Hz, a minimum *NET* of $0.5 \mu\text{K}/\text{Hz}^{1/2}$, among the investigated film thicknesses, is obtained for the 105 nm thick resonator [see Fig. 4(b)].

The temperature resolution below 1 Hz seems to be limited by low-frequency fluctuations in the order of 100 μK , as shown in Fig. 4(c). The origin of such fluctuations is investigated by means of an experiment where two resonators are simultaneously measured (the 147 nm and the 105 nm thick ones). As fully described in the [supplementary material](#), the two S-SRRs are individually excited by the same GCPW at their corresponding resonance frequencies (*i.e.* 1.1394 GHz and 1.1371 GHz, respectively) by two distinct microwave generators, modulating their excitations by two distinct modulation frequencies (*i.e.* 11 kHz and 18 kHz, respectively). Two lock-in amplifiers are used to perform the FM synchronous demodulation. Once normalized to the respective temperature responsivities $R(4.2 \text{ K})$, the responses of the two sensors show an almost identical time evolution, indicating that such low-frequency fluctuations might originate from a global common

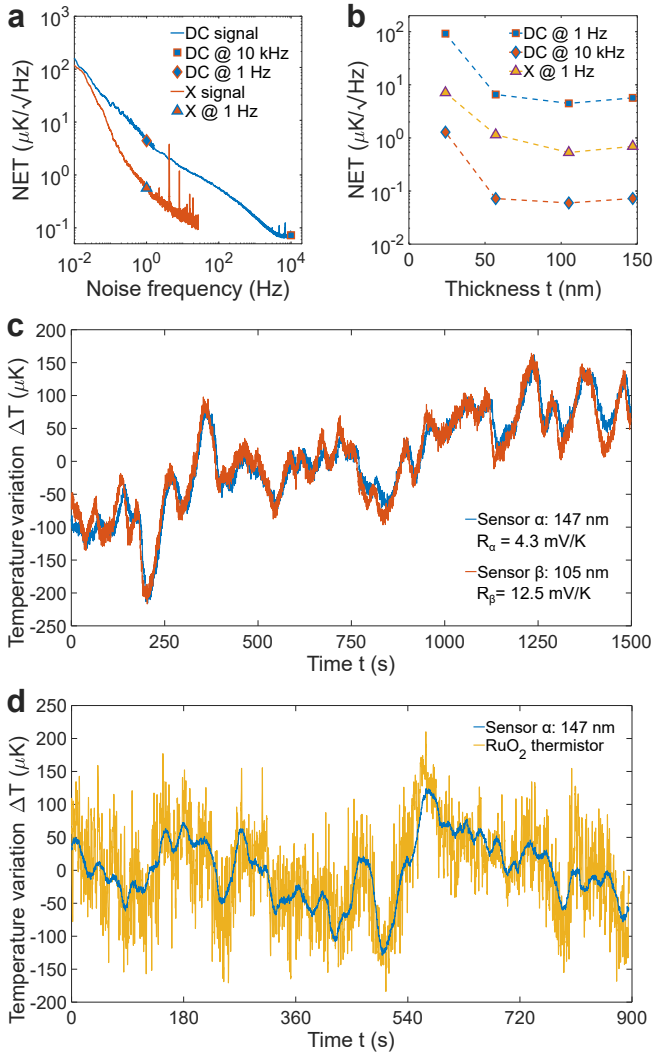


FIG. 4. Noise characterization of the different S-SRRs at 4.2 K. a) Frequency spectra of the NET for the 147 nm thick resonator. b) Noise equivalent temperatures of the different S-SRRs, evaluated in DC, both at 10 kHz (blue-square points) and 1 Hz (orange-diamond points), and in AC, at 1 Hz (yellow-triangle points). c) 25 min time-lapse simultaneous temperature monitoring of the two X signals associated to two different S-SRRs. d) 15 min time-lapse evolution of the simultaneous temperature recording by one S-SRR sensor and a commercial RuO_2 thermistor.

physical stimulus rather than from a noise source intrinsic to each sensor. Additionally, the coincidence of the two temperature estimations, originating from two sensors having significantly different responsivities, suggests the signal variations are associated to temperature-related phenomena. These hypotheses are confirmed by a final experiment, where the temperature inside the LHe dewar is simultaneously monitored by means of the 147 nm thick S-SRR and a commercial sensor relying on a different physical principle, in particular a RuO_2 thermistor⁵⁶. As shown in Fig. 4(d), the thermistor response follows the resonator, especially over the largest fluctuations around $100 \mu\text{K}$. The technical details concerning this experiment are reported in the [supplementary material](#).

In conclusion, we have fabricated and tested a set of temperature-sensitive $\text{Nb}_{50}\text{Ti}_{50}$ superconducting S-SRRs, generally showing $Q_L > 10^4$ for $3 \text{ K} < T < 10 \text{ K}$, in order to investigate the influence of the thin-film thickness on the resonance frequency shifts induced by the change of their kinetic inductance $L_K(T)$. In particular, the 24 nm thinnest device exhibits the highest temperature sensitivity of 19 MHz/K , due to its larger value of surface kinetic inductance. However, the significant reduction in the loaded quality factor for thinner films entails a reduction of the maximum slope for the sensing DC and X curves, inducing an optimum condition at intermediate thickness values, when evaluating the temperature resolution of the devices. In this perspective, we have exploited frequency modulation and lock-in detection to assess the possibility to reach a sub- μK temperature resolution for such devices. The possibility to excite different resonators with the same microwave transmission line, while simultaneously tracking their temperature responses, have also been successfully demonstrated. Noise equivalent temperatures as low as $0.5 \mu\text{K}/\text{Hz}^{1/2}$ are reported at 1 Hz in liquid He for a 105 nm thick S-SRR. We believe that such superconducting devices, eventually benefiting from higher kinetic inductance films and entailing multiplexed readout schemes, could find applications in the measurement of distributed on-chip cryogenic temperatures.

SUPPLEMENTARY MATERIAL

The [supplementary material](#) contains additional information about the following topics:

- S1. Microfabrication process flow and SEM/AFM characterization of the patterned S-SRRs;
- S2. FEM microwave simulation of the resonance mode for the 1.1 GHz S-SRR geometry;
- S3. Experimental determination of the S-SRR-to-GCPW coupling distance d_{cpl} in a LHe dewar;
- S4. VTI temperature calibration of the S-SRRs;
- S5. Determination of the modulation P_{RF} , Δf_{FM} and f_{FM} parameters in a LHe dewar;
- S6. Simultaneous temperature monitoring in a LHe dewar, by means of two different S-SRRs;
- S7. Simultaneous temperature monitoring in a LHe dewar, by means of an S-SRR and a RuO_2 thermistor.

ACKNOWLEDGEMENTS

The authors thank the EPFL Center of Micro/Nanotechnology (CMi), in particular Cyrille Hibert, Julien Dorsaz, Niccolò Piacentini, Joffrey Pernollet and Adrien Toros, for the facility support provided during the microfabrication processing. We would also like to acknowledge Nergiz Sahin-Solmaz and Biranche Tandon for the fruitful discussions. This work has received funding from the Swiss National Science Foundation (SNSF), under the AMBIZIONE program (Project "Cryogenic Thermometry based on Superconducting Microwave Resonators", grant agreement No. PZ00P2_193361).

DATA AVAILABILITY

The data that support the findings of this study are available from the corresponding author upon reasonable request.

CREDITS

The following article has been submitted to *Applied Physics Letters*. After it is published, it will be found at [Link](#).

REFERENCES

- ¹M. D. Audley, R. L. Kelley, and G. L. Rawley, “A prototype kinetic inductance thermometer for X-ray calorimetry,” *J. Low. Temp. Phys.* **93**, 245–250 (1993).
- ²P. K. Day, H. G. LeDuc, B. A. Mazin, A. Vayonakis, and J. Zmuidzinas, “A broadband superconducting detector suitable for use in large arrays,” *Nature* **425**, 817–821 (2003).
- ³P. R. Maloney, N. G. Czakon, P. K. Day, T. P. Downes, R. Duan, J. Gao, J. Glenn, S. R. Golwala, M. I. Hollister, H. G. LeDuc, B. A. Mazin, S. G. McHugh, O. Noroozian, H. T. Nguyen, J. Sayers, J. A. Schlaerth, S. Siegel, J. E. Vaillancourt, A. Vayonakis, P. Wilson, and J. Zmuidzinas, “MUSIC for sub/millimeter astrophysics,” in *Millimeter, Submillimeter, and Far-Infrared Detectors and Instrumentation for Astronomy V*, Vol. 7741 (2010) p. 77410F.
- ⁴J. E. Austerlmann, J. A. Beall, S. A. Bryan, B. Dober, J. Gao, G. Hilton, J. Hubmayr, P. Mauskopf, C. M. McKenney, S. M. Simon, J. N. Ullom, M. R. Vissers, and G. W. Wilson, “Millimeter-wave polarimeters using kinetic inductance detectors for ToITeC and beyond,” *J. Low. Temp. Phys.* **193**, 120–127 (2018).
- ⁵K. Dibert, P. Barry, Z. Pan, A. Anderson, B. Benson, C. Chang, K. Karkare, J. Li, T. Natoli, M. Rouble, E. Shirokoff, A. Stark, and the South Pole Telescope Collaboration, “Development of MKIDs for measurement of the cosmic microwave background with the South Pole Telescope,” *J. Low. Temp. Phys.* **209**, 363–371 (2022).
- ⁶A. Wallraff, D. I. Schuster, A. Blais, L. Frunzio, R.-S. Huang, J. Majer, S. Kumar, S. M. Girvin, and R. J. Schoelkopf, “Strong coupling of a single photon to a superconducting qubit using circuit quantum electrodynamics,” *Nature* **431**, 162–167 (2004).
- ⁷M. Göppl, A. Fragner, M. Baur, R. Bianchetti, S. Filipp, J. M. Fink, P. J. Leek, G. Puebla, L. Steffen, and A. Wallraff, “Coplanar waveguide resonators for circuit quantum electrodynamics,” *J. Appl. Phys.* **104**, 113904 (2008).
- ⁸P. Scarlino, D. J. van Woerkom, A. Stockklauser, J. V. Koski, M. C. Colloido, S. Gasparinetti, C. Reichl, W. Wegscheider, T. Ihn, K. Ensslin, and A. Wallraff, “All-microwave control and dispersive readout of gate-defined quantum dot qubits in circuit quantum electrodynamics,” *Phys. Rev. Lett.* **122**, 206802 (2019).
- ⁹M. Kjaergaard, M. E. Schwartz, J. Braumüller, P. Krantz, J. I.-J. Wang, S. Gustavsson, and W. D. Oliver, “Superconducting qubits: current state of play,” *Annu. Rev. Condens. Matter Phys.* **11**, 369–395 (2020).
- ¹⁰J. Koch, T. M. Yu, J. Gambetta, A. A. Houck, D. I. Schuster, J. Majer, A. Blais, M. H. Devoret, S. M. Girvin, and R. J. Schoelkopf, “Charge-insensitive qubit design derived from the Cooper pair box,” *Phys. Rev. A* **76**, 042319 (2007).
- ¹¹J. A. Schreier, A. A. Houck, J. Koch, D. I. Schuster, B. R. Johnson, J. M. Chow, J. M. Gambetta, J. Majer, L. Frunzio, M. H. Devoret, S. M. Girvin, and R. J. Schoelkopf, “Suppressing charge noise decoherence in superconducting charge qubits,” *Phys. Rev. B* **77**, 180502 (2008).
- ¹²R. Barends, J. Kelly, A. Megrant, A. Veitia, D. Sank, E. Jeffrey, T. C. White, J. Mutus, A. G. Fowler, B. Campbell, Y. Chen, Z. Chen, B. Chiaro, A. Dunsworth, C. Neill, P. O’Malley, P. Roushan, A. Vainsencher, J. Wenner, A. N. Korotkov, A. N. Cleland, and J. M. Martinis, “Superconducting quantum circuits at the surface code threshold for fault tolerance,” *Nature* **508**, 500–503 (2014).
- ¹³M. R. Vissers, R. P. Erickson, H.-S. Ku, L. Vale, X. Wu, G. C. Hilton, and D. P. Pappas, “Low-noise kinetic inductance traveling-wave amplifier using three-wave mixing,” *Appl. Phys. Lett.* **108**, 012601 (2016).
- ¹⁴J. Aumentado, “Superconducting parametric amplifiers: the state of the art in Josephson parametric amplifiers,” *IEEE Microw. Mag.* **21**, 45–59 (2020).
- ¹⁵S. Frasca, C. Roy, G. Beaulieu, and P. Scarlino, “Three-wave-mixing quantum-limited kinetic inductance parametric amplifier operating at 6 T near 1 K,” *Phys. Rev. Appl.* **21**, 024011 (2024).
- ¹⁶A. Bienfait, J. J. Pla, Y. Kubo, M. Stern, X. Zhou, C. C. Lo, C. D. Weis, T. Schenkel, M. L. W. Thewalt, D. Vion, D. Esteve, B. Julsgaard, K. Mølmer, J. J. L. Morton, and P. Bertet, “Reaching the quantum limit of sensitivity in electron spin resonance,” *Nat. Nanotechnol.* **11**, 253–257 (2016).
- ¹⁷V. Ranjan, S. Probst, B. Albanese, T. Schenkel, D. Vion, D. Esteve, J. J. L. Morton, and P. Bertet, “Electron spin resonance spectroscopy with femto-liter detection volume,” *Appl. Phys. Lett.* **116**, 184002 (2020).
- ¹⁸Y. Artzi, Y. Yishay, M. Fanciulli, M. Jbara, and A. Blank, “Superconducting micro-resonators for electron spin resonance - the good, the bad, and the future,” *J. Mag. Res.* **334**, 107102 (2021).
- ¹⁹D. Akhmetzhanov, T. W. Borneman, I. Taminiau, S. Sadeghi, H. R. Mohebbi, and D. G. Cory, “Electron spin resonance spectroscopy using a Nb superconducting resonator,” *Appl. Phys. Lett.* **123**, 224002 (2023).
- ²⁰S. S. Courts and P. R. Swinehart, “Review of Cernox™ (Zirconium Oxynitride) Thin-Film Resistance Temperature Sensors,” *AIP Conf. Proc.* **684**, 393–398 (2003).
- ²¹S. A. Myers, H. Li, and G. A. Csáthy, “A ruthenium oxide thermometer for dilution refrigerators operating down to 5 mK,” *Cryogenics* **119**, 103367 (2021).
- ²²D. S. Holmes and S. S. Courts, “Resolution and accuracy of cryogenic temperature measurements,” *Temperature: Its Measurement and Control in Science and Industry* **6**, 1225–1230 (1992).
- ²³C. J. Yeager and S. S. Courts, “A review of cryogenic thermometry and common temperature sensors,” *IEEE Sens. J.* **1**, 352–360 (2001).
- ²⁴G. M. Noah, T. H. Swift, M. de Kruijf, A. Gomez-Saiz, J. J. L. Morton, and M. F. Gonzalez-Zalba, “CMOS on-chip thermometry at deep cryogenic temperatures,” *Appl. Phys. Rev.* **11**, 021414 (2024).
- ²⁵J. Wheeler, M. R. Vissers, M. Malnou, J. Hubmayr, J. N. Ullom, and J. Gao, “Sub-kelvin thermometer for on-chip measurements of microwave devices utilizing two-level systems in superconducting microresonators,” *Appl. Phys. Lett.* **117**, 192601 (2020).
- ²⁶H. Yu, L. Jing, T. Hua, and W. Xu, “Temperature and power characteristics of quarter-wavelength superconducting coplanar waveguide resonator,” *SN Appl. Sci.* **4**, 67 (2022).
- ²⁷L. Nulens, N. Lejeune, J. Caeyers, S. Marinković, I. Cools, H. Dausy, S. Basov, B. Raes, M. J. Van Bael, A. Geresdi, A. V. Silhanek, and J. Van de Vondel, “Catastrophic magnetic flux avalanches in NbTiN superconducting resonators,” *Commun. Phys.* **6**, 267 (2023).
- ²⁸C. J. Gorter and H. Casimir, “On supraconductivity I,” *Physica* **1**, 306–320 (1934).
- ²⁹K. Watanabe, K. Yoshida, and T. A. Kohjiro, “Kinetic inductance of superconducting coplanar waveguides,” *Jpn. J. Appl. Phys.* **33**, 5708 (1994).
- ³⁰M. A. Hein, “Microwave properties of superconductors,” in *Microwave superconductivity*, edited by H. Weinstock and M. Nisenoff (Springer Netherlands, Dordrecht, 2001) pp. 21–53.
- ³¹M. Tinkham, *Introduction to superconductivity*, 2nd ed. (Dover, Mineola, N.Y., 2004).
- ³²A. J. Annunziata, D. F. Santavica, L. Frunzio, G. Catelani, M. J. Roeks, A. Frydman, and D. E. Prober, “Tunable superconducting nanoinductors,” *Nanotechnol.* **21**, 445202 (2010).
- ³³Y. F. Bychkov, R. Herzog, and I. S. Khukhareva, “Thermal conductivity and electrical resistivity of NbTi alloys at low temperatures,” *Cryogenics* **21**, 741–745 (1981).
- ³⁴L. Bottura, “A practical fit for the critical surface of NbTi,” *IEEE Trans. Appl. Supercond.* **10**, 1054–1057 (2000).
- ³⁵G. Ghigo, D. Torsello, L. Gozzelino, M. Fracasso, M. Bartoli, C. Pira, D. Ford, G. Marconato, M. Fretto, I. De Carlo, N. Pompeo, and E. Silva, “Vortex dynamics in NbTi films at high frequency and high DC magnetic fields,” *Sci. Rep.* **13**, 9315 (2023).
- ³⁶R. Russo, A. Chatel, N. Sahin Solmaz, R. Farsi, H. Furci, J. Brugger, and G. Boero, “Fabrication and characterization of NbTi microwave superconducting resonators,” *Micro Nano Eng.* **19**, 100203 (2023).
- ³⁷C. Benvenuti, S. Calatroni, M. Hauer, M. Minestrini, G. Orlandi, and W. Weingarten, “(NbTi)N and NbTi coatings for superconducting accelerating cavities,” in *5th Workshop on Radio-frequency Superconductivity* (1991) pp. 518–526.
- ³⁸Z. Charifoulline, “Residual resistivity ratio (RRR) measurements of LHC

- superconducting NbTi cable strands,” *IEEE Trans. Appl. Supercond.* **16**, 1188–1191 (2006).
- ³⁹P. Zhang, J. Li, G. Q., Y. Zhu, K. Yan, R. Wang, K. Zhang, X. Liu, and Y. Feng, “Chapter 15 - NbTi superconducting wires and applications,” in *Titanium for consumer applications* (Elsevier, 2019) pp. 279–296.
- ⁴⁰S. N. Buckley, P. Agnew, and G. P. Pells, “Cryogenic dielectric properties of sapphire at 2.45 GHz,” *J. Phys. D: Appl. Phys.* **27**, 2203 (1994).
- ⁴¹J. Krupka, K. Derzakowski, M. Tobar, J. Hartnett, and R. G. Geyer, “Complex permittivity of some ultralow loss dielectric crystals at cryogenic temperatures,” *Meas. Sci. Technol.* **10**, 387 (1999).
- ⁴²N. Pogue, P. McIntyre, A. Sattarov, and C. Reece, “Measurement of the dielectric properties of high-purity sapphire at 1.865 GHz from 2–10 Kelvin,” *AIP Conf. Proc.* **1434**, 945–952 (2012).
- ⁴³C. X. Yu, S. Zihlmann, G. Troncoso Fernández-Bada, J.-L. Thomassin, F. Gustavo, E. Dumur, and R. Maurand, “Magnetic field resilient high kinetic inductance superconducting niobium nitride coplanar waveguide resonators,” *Appl. Phys. Lett.* **118**, 054001 (2021).
- ⁴⁴D. J. Parker, M. Savytskyi, W. Vine, A. Laucht, T. Duty, M. Morello, A. L. Grimsom, and J. J. Pla, “Degenerate parametric amplification via three-wave mixing using kinetic inductance,” *Phys. Rev. Appl.* **17**, 034064 (2022).
- ⁴⁵S. Frasca, I. N. Arabadzhiev, S. Y. B. de Puechredon, F. Oppliger, V. Jouanny, R. Musio, M. Scigliuzzo, F. Minganti, P. Scarlino, and E. Charbon, “NbN films with high kinetic inductance for high-quality compact superconducting resonators,” *Phys. Rev. Appl.* **20**, 044021 (2023).
- ⁴⁶A. K. Horestani, M. Durán-Sindreu, J. Naqui, C. Fumeaux, and F. Martín, “Coplanar waveguides loaded with S-Shaped Split-Ring Resonators: modeling and application to compact microwave filters,” *IEEE Antennas Wirel. Propag. Lett.* **13**, 1349–1352 (2014).
- ⁴⁷C. Herrojo, J. Naqui, F. Paredes, and F. Martín, “Spectral signature barcodes based on S-Shaped Split Ring Resonators (S-SRRs),” *EPJ Appl. Metamater.* **3**, 1 (2016).
- ⁴⁸A. K. Horestani, N. Varmazyar, F. Sadeghikia, M. T. Noghani, Z. Shaterian, and F. Martín, “On the applications of S-Shaped Split Ring Resonators (S-SRR) in sensors, filters, and antennas,” in *2019 International Conference on Electromagnetics in Advanced Applications (ICEAA)* (2019) pp. 0485–0488.
- ⁴⁹R. R. Mansour, “Microwave superconductivity,” *IEEE Trans. Microw. Theory Tech.* **50**, 750–759 (2002).
- ⁵⁰D. Hafner, M. Dressel, and M. Scheffler, “Surface-resistance measurements using superconducting stripline resonators,” *Rev. Sci. Instrum.* **85**, 014702 (2014).
- ⁵¹D. S. Rausch, M. Thiemann, M. Dressel, D. Bothner, D. Koelle, R. Kleiner, and M. Scheffler, “Superconducting coplanar microwave resonators with operating frequencies up to 50 GHz,” *J. Phys. D: Appl. Phys.* **51**, 465301 (2018).
- ⁵²J. Gao, *The physics of superconducting microwave resonators*, PhD thesis, California Institute of Technology (2008).
- ⁵³M. Takeda and K. Nishigaki, “Magnetic field dependence of critical current density of NbTi thin films as a parameter of angle,” in *Advances in Superconductivity XI* (1999) pp. 533–536.
- ⁵⁴J. Gao, J. Zmuidzinas, B. A. Mazin, H. G. LeDuc, and P. K. Day, “Noise properties of superconducting coplanar waveguide microwave resonators,” *Appl. Phys. Lett.* **90**, 102507 (2007).
- ⁵⁵S. Kumar, J. Gao, J. Zmuidzinas, B. A. Mazin, H. G. LeDuc, and P. K. Day, “Temperature dependence of the frequency and noise of superconducting coplanar waveguide resonators,” *Appl. Phys. Lett.* **92**, 123503 (2008).
- ⁵⁶G. G. Ihas, L. Frederick, and J. P. McFarland, “Low temperature thermometry in high magnetic fields,” *J. Low Temp. Phys.* **113**, 63–968 (1998).

Thin-film superconducting NbTi microwave resonators for cryogenic thermometry: Supplementary material

A. Chatel,¹ R. Russo,¹ L. Mazzone,¹ Q. Boinay,¹ R. Farsi,¹ J. Brugger,¹ G. Boero¹⁻² and H. Furci¹

¹Microsystems Laboratory, EPFL, 1015 Lausanne, Switzerland

²Center for Quantum Science and Engineering, EPFL, 1015 Lausanne, Switzerland

S1 Microfabrication of the superconducting S-SRRs

This section is dedicated to the description of the microfabrication of the S-shaped split ring resonators (S-SRRs). In Fig. S1 we schematize the process flow to pattern Nb₅₀Ti₅₀ thin-films (with thickness values approximatively ranging from 20 nm to 150 nm) on top of 650 μ m thick C-plane sapphire wafers. The first two steps involve the deposition of a backside 10 nm-100 nm Ti-Al bilayer (necessary to perform an electrostatic wafer clamping during the plasma etching process) and the superconducting Nb₅₀Ti₅₀ front layer. In both cases, the materials are DC sputtered on the sapphire substrate, kept at room temperature. Two consecutive runs of direct laser writing photolithography ($\lambda = 355$ nm) followed by two different dry etching processes are, then, performed in order to pattern the S-SRR resonators. In particular, the first high-resolution process exploits a fluorine-based plasma etching to pattern the S-SRR geometries in small squared openings. As a matter of fact, when the design pattern consists of large regions exposed to plasma, electrostatic de-clamp of the wafer frequently occurs, attributed to a significant deformation of the sapphire substrate, probably due to the thin-film stress induced by a large temperature increase during the etching process. This issue is avoided when the area of the open regions is limited to the minimum around the highly resolved resonator patterns. The second lithography-etching run, relying on the use of Ar-ion beam milling, is necessary to remove the remaining metallic layer. Indeed, the edge-clamping mechanism of our milling machine is exclusively mechanical, preventing any wafer de-clamp due to thermal stress and overheating. The use of the plasma etching over this latter technique is preferred due to the loss of resolution and wall sharpness induced by the thermal reflow of the photoresist. In the end, the wafer is diced into 12.5 mm \times 8.5 mm rectangular chips, each containing two different S-SRRs. The presence of two resonators, showing a similar geometry but a significant difference in overall sizes, has to be attributed to our initial intention to perform a simultaneous frequency-multiplexed readout in different regions of the microwave spectrum.

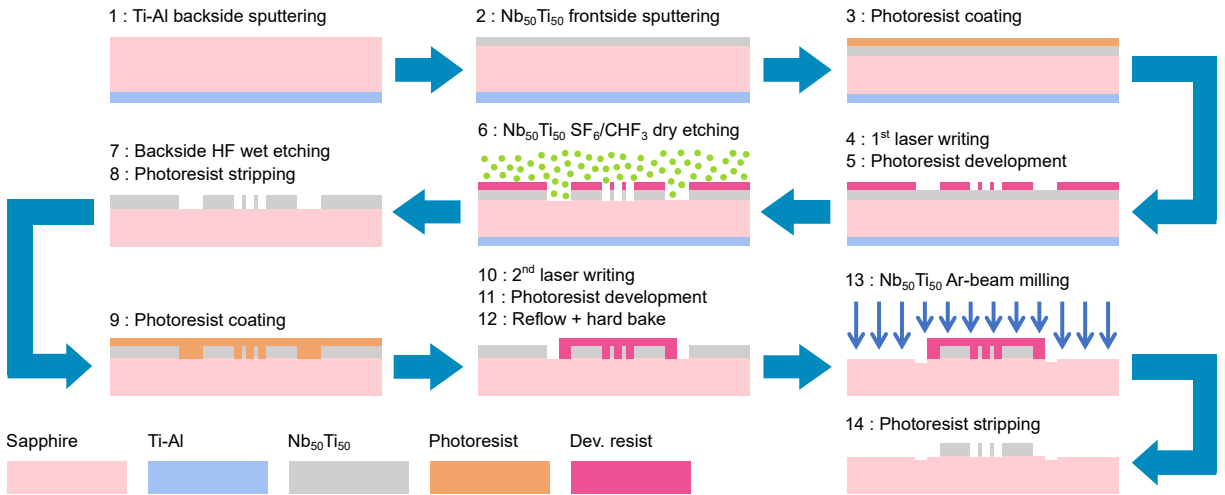


Figure S1: Microfabrication process flow to pattern Nb₅₀Ti₅₀ thin-films on top of sapphire wafers.

Fig. S2 reports the main results concerning the patterning quality of the fabricated devices. Each diced chip contains two resonators [see Fig. S2(a)], the smallest and the largest ones designed to respectively resonate around 1.6 GHz and 1.1 GHz. Considering the S-SRR geometry of this latter, being the only device under test (DUT) analyzed all over this work, the critical dimensions of such a design are related to the interdigitated finger capacitors (finger length : 148 μ m, finger width: 4 μ m, inter-finger gap: 2 μ m). Even though scanning electron microscopy (SEM) pictures allow to assess

the quality of the overall microfabrication, confirming the absence of major defects [see Fig. S2(b-c)], atomic force microscopy (AFM) scans quantitatively estimate the pattern accuracy. In particular, from Fig. S2(d-e) it is possible to determine the design transfer inaccuracy of the patterned features, lower than 300 nm, as well as the exact film thickness attained through the Nb₅₀Ti₅₀ thin-film sputtering. Similar measurements are carried out on each of the samples fabricated for this work.

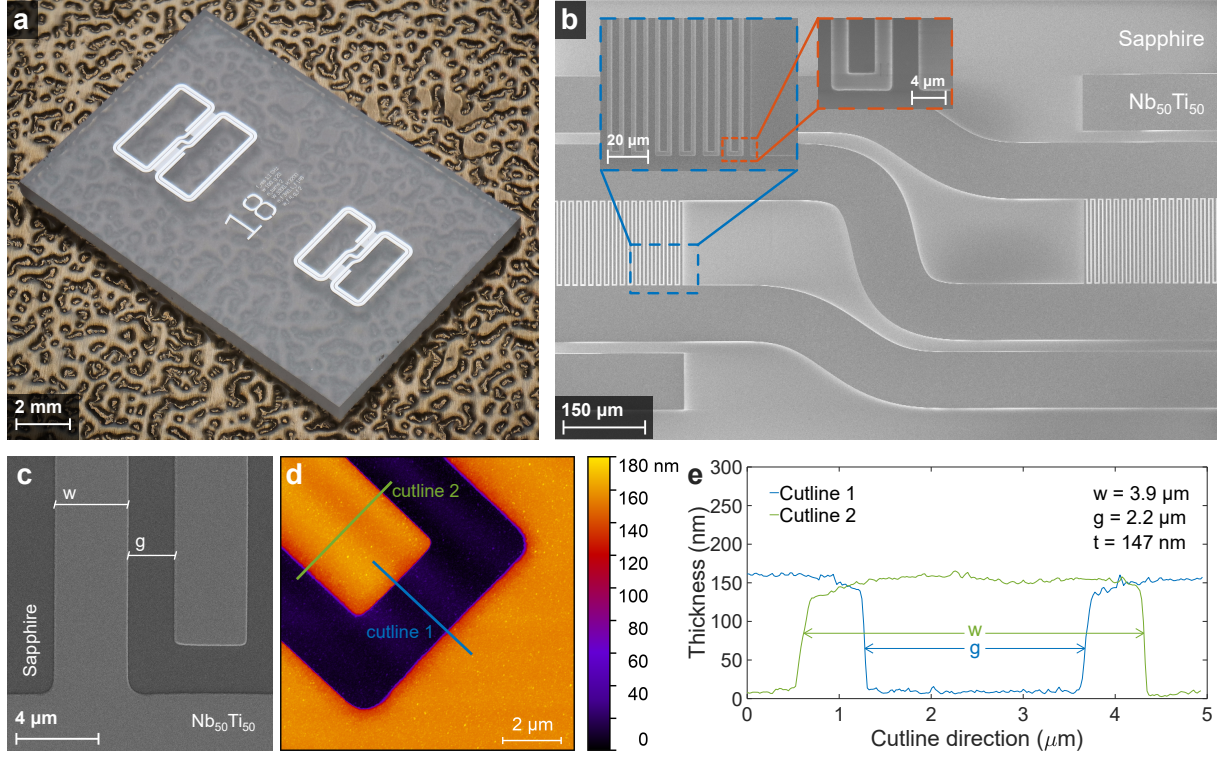


Figure S2: Characterization of the microfabrication process flow. a) Optical microscope picture of the sapphire chip: the DUT corresponds to the top-left resonator. b) Set of SEM images, zooming on the interdigitated fingers region of the S-SRR. c) SEM picture highlighting some fingers of the IDC. d) AFM zoomed scan of the previous structure: the Nb₅₀Ti₅₀ film is supposed to be 150 nm thick by design. e) AFM cross-section cuts of a single finger, along its width and gap size.

S2 Microwave simulation of the GCPW-coupled S-SRRs

The aim of this section is to present the electromagnetic simulation of the proposed S-SRR geometry. COMSOL Multiphysics® and, specifically, its *Electromagnetic Waves, Frequency Domain (emw)* environment are exploited to estimate the resonance frequency of the thin-film microresonator, coupled to the microwave grounded coplanar waveguide (GCPW). Fig. S3(a) presents the schematic of the simulated 2-port geometry. A microwave power is injected from port 1 on the left and collected at port 2 on the right. The resonator is placed face-down at a 2.5 mm coupling distance d_{cpl} . Because of the extremely low aspect ratio of the device, the Nb₅₀Ti₅₀ film is simulated as a bi-dimensional perfect electric conductor (PEC). This simplification does not allow to study the superconducting RF properties of the film, but it results to be sufficiently accurate and computationally efficient to estimate the resonance frequency of the device to be around 1.1 GHz. For such a geometry, the total geometric inductance is estimated by analytical expressions^{1,2} as $L_G \sim 39$ nH. By knowing the resonance frequency value from simulation, the total geometric capacitance is calculated as $C_G = 1/((2\pi f)^2 L_G) \sim 570$ fF. The GCPW port-matching is also evaluated for the propagation quasi-TEM mode, getting a characteristic impedance $Z_C = 48 \Omega$. The characteristic S-SRR eigenmode is properly excited by the GCPW antisymmetric magnetic field configuration, allowing the resonator to inductively couple to the transmission line. [see Fig. S3(b-c)].

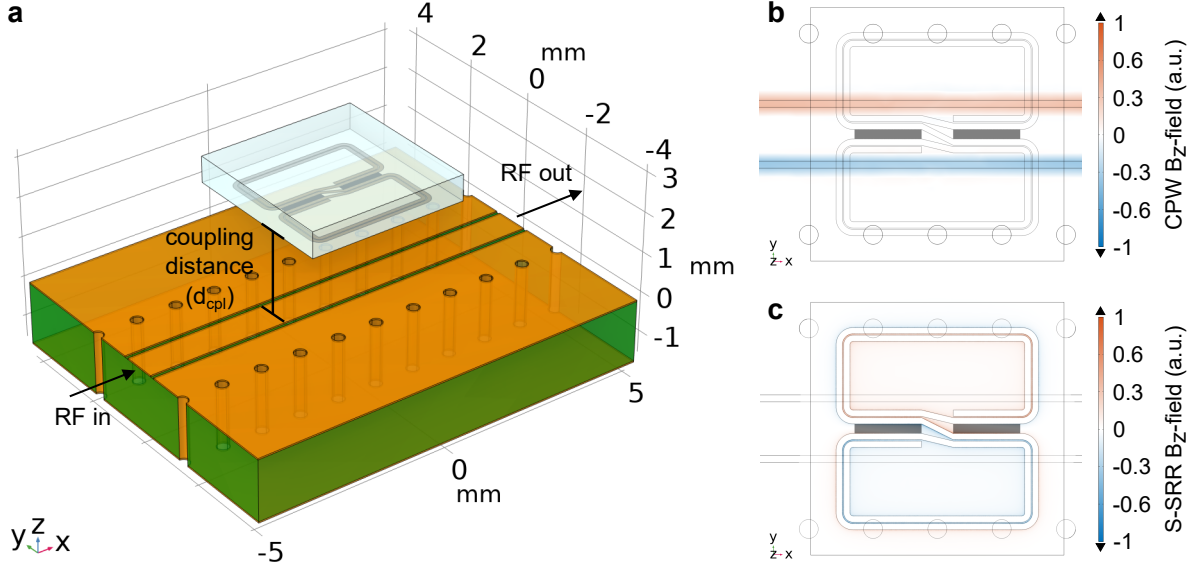


Figure S3: COMSOL Multiphysics® electromagnetic microwave simulation of the S-SRR excited by a GCPW. a) Schematic presenting the simulated 2-port geometry. The GCPW consists of a $34\text{ }\mu\text{m}$ thick copper plate on top of a 1.5 mm thick ROGERS 4003C™ laminate ($\epsilon_r \simeq 3.38$ and $\tan\delta \simeq 0.003$). The central signal line is $850\text{ }\mu\text{m}$ wide and $110\text{ }\mu\text{m}$ laterally spaced from the ground plane. b-c) Antisymmetric magnetic field distribution of the GCPW, exciting the characteristic resonance S-SRR mode.

S3 Determination of the coupling condition

In this section, we report on the preliminary test implemented to experimentally determine a suitable coupling condition between the S-SRRs and the GCPW. A 147 mm thick device is tested at a fixed 4.2 K temperature, inside a liquid He (LHe) dewar. The same resonator chip is successively characterized at different distances from the same GCPW printed circuit board (PCB), by changing the 3D-printed spacer. The system is excited in a 2-port scheme directly through a VNA (*PicoVNA 108*), with a -18 dBm input power, performing a frequency sweep to locate the resonance condition. The data are successively fitted to a skewed-Lorentzian model³ in order to extract the quality factor of the resonator for each coupling distance. Fig. S4 shows the most important figures-of-merit concerning this specific characterization. The loaded Q-factor tends to saturate, with respect to the distance, to values as high as 2.58×10^4 , while the peak depth degrades, proving a gradually lower transfer of energy to the resonator as d_{cpl} increases. Basing on this preliminary characterization, we chose a coupling distance value of 2.5 mm , in order to excite the resonator with approximately 50% of the transmitted power (background: $S_{21} = 0.82$; in-resonance: $S_{21} = 0.56$), still preserving a Q-factor larger than half the saturation condition (i.e. $Q_L(2.5\text{ mm}) = 1.75 \times 10^4$). Such a choice allows us to clearly isolate and distinguish resonance peaks for further variable-temperature characterizations.

S4 Temperature calibration of the S-SRRs

The aim of this section is to present the procedure exploited to perform the temperature calibration of the S-SRRs. The temperature monitoring and control is achieved through the use of two CERNOX® thermometers and two heaters. The thermometer-heater couple closest to the microwave resonator is mounted at about 20 mm from the two microwave connectors on the PCB [see Fig. S5(a-b)]. The ground electrical connection of these latter is in thermal contact with a 4 cm^3 copper block on which the thermometer and the heater are mounted. The other couple is mounted on the bottom of the VTI and is used to control the temperature of the He gas flowing around the resonator. Typically this temperature is set 0.2 K below the desired one in proximity of the device and measured with the other thermometer.

Moreover, the front side of the PCB is connected, in transmission, to two BeCu coaxial cables, used to excite the superconducting sensor placed 2.5 mm far from the surface, while its back side is dedicated to the DC routing to perform the cryogenic characterization of the thin-film. Additionally, as shown in Fig. S5(c), in order to reduce the influence of external magnetic fields, the whole system, comprising of the sensing S-SRR and excitation PCB, is encapsulated in a cylindrical magnetic shield (from *Magnetic Shields Ltd*) made of CRYOPHY®, a Ni-Fe soft magnetic alloy typically exploited to shield magnetic fields in cryogenic environments (μ_r around 7×10^4 at 4 K).

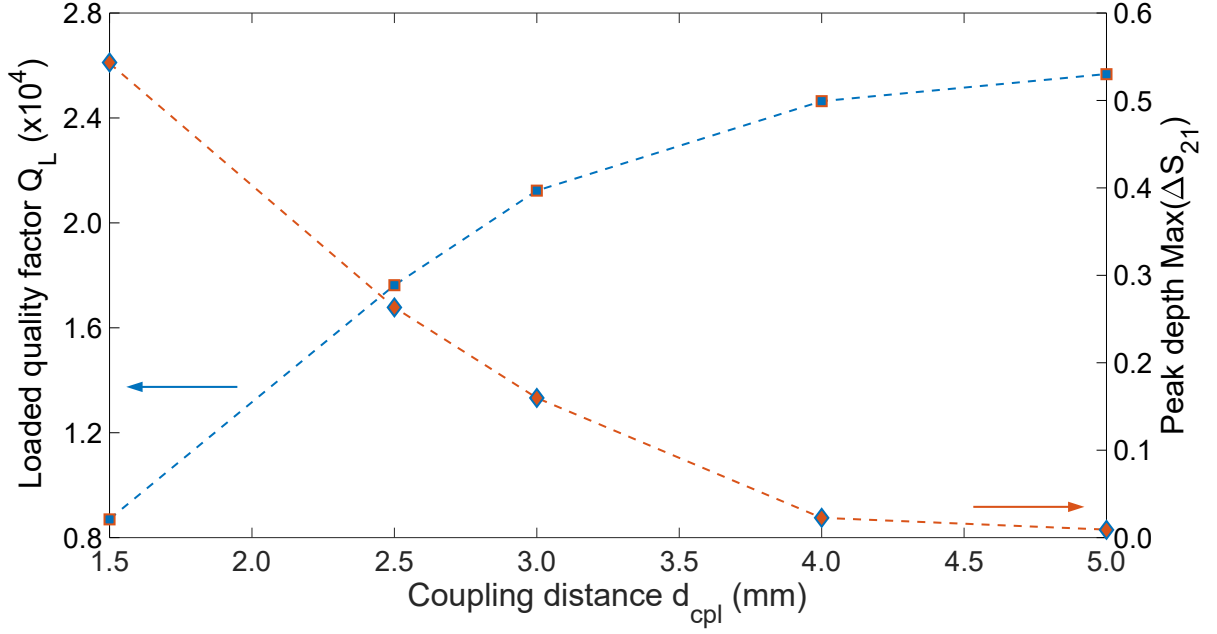


Figure S4: Experimental search for an optimal resonator-to-GCPW coupling distance. The dashed blue line represents the evolution of the loaded Q-factor, while the orange curve corresponds to the skewed-Lorentzian peak depth.

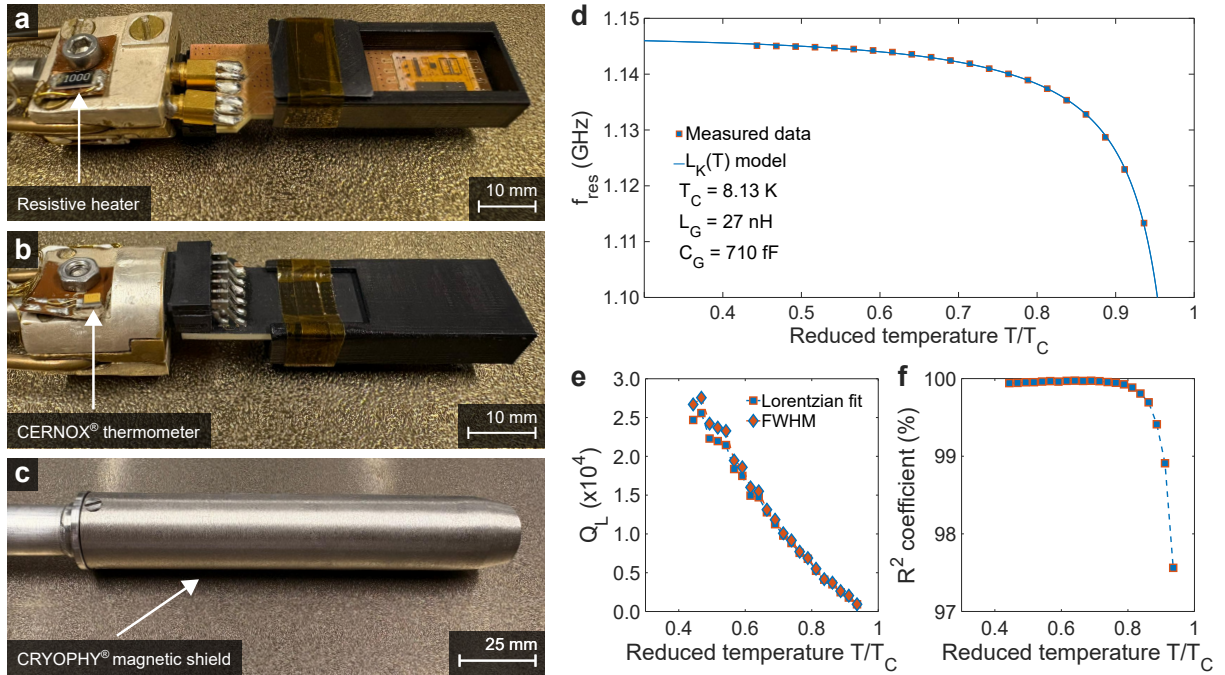


Figure S5: Temperature calibration of the superconducting S-SRRs. a) Front side of the PCB, connected to the cryogenic probe. The resistive heater, exploited for controlling the temperature, is shown on the left. b) Back side of the PCB, connected to the cryogenic probe. The CERNOX[®] thermometer, exploited for measuring the chip temperature, is shown on the left. c) Bottom extremity of the cryogenic probe, enclosed by the CRYOPHY[®] magnetic shield. d) Typical temperature evolution of the resonance frequency, for the 147 nm thick resonator. The squared points represent the measured data, while the continuous line stands for the $L_K(T)$ model. e) Temperature dependence of the loaded Q-factor. f) R^2 skewed-Lorentzian fitting coefficient for each frequency scan at different temperatures.

Fig. S5(d) presents the evolution of the resonance frequency of a single S-SRR, 147 nm thick. The Cu GCPW is excited through a VNA (*PicoVNA 108*), directly connected in transmission to the PCB by BeCu coaxial cables, delivering a microwave power of -18 dBm. Frequency scans are collected at different temperatures and, then, fitted to a skewed-Lorentzian model³ for extracting the resonance frequency and loaded quality factor values. The temperature variation of f_{res} is additionally fitted to a kinetic inductance-based model^{4,5,6}, showing a good agreement with the acquired data and the estimation of the T_C , L_G and C_G fitting parameters. In Fig. S5(e) we report the temperature dependence of the loaded quality factor Q_L , estimated both by means of the skewed-Lorentzian model and by the resonating full width at half maximum (FWHM) definition $f_{res}/\Delta f_{FWHM}$. The two definitions show very similar results for Q_L over the entire temperature range. The goodness of the resonance deep fitting is also demonstrated by the R^2 parameter, larger than 99.9% for the majority of the frequency scans (*i.e.* $T/T_C < 0.8$) and in any case better than 97%, only degrading close to the thin-film critical temperature T_C [see Fig. S5(f)].

S5 Determination of the modulation parameters

This section is dedicated to the description of the setup used to characterize the noise equivalent temperature (*NET*) of the resonators, in liquid He at 4.2 K, as well as the preliminary tests carried out to identify the optimal modulation parameters for performing such an estimation of the temperature resolution.

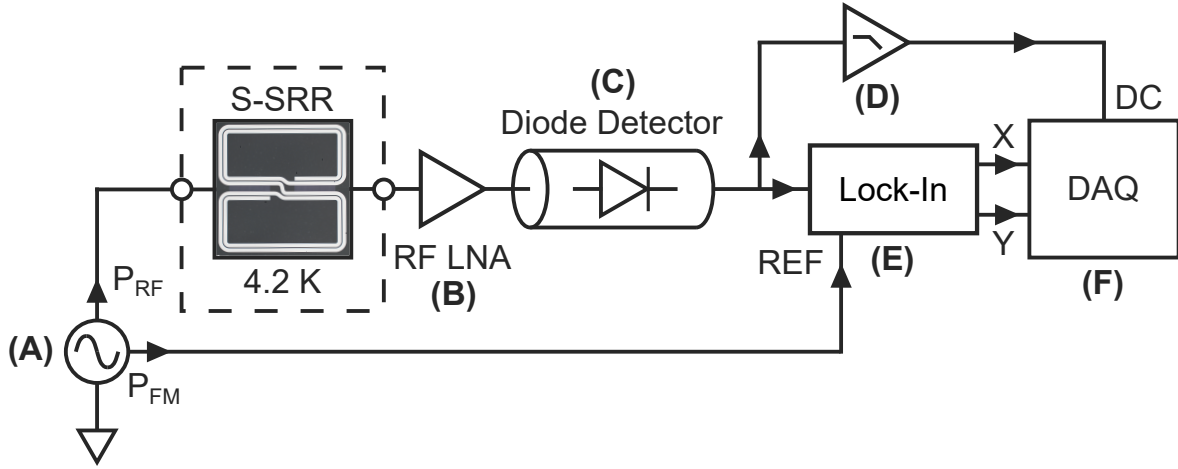


Figure S6: Instrumentation setup exploited to extract the *NET* of the different S-SRRs in liquid He at 4.2 K.

Fig. S6 schematically depicts the instrumentation setup. First, a microwave signal generator (A. *Stanford Research SG384*) is exploited to excite the S-SRR with a power P_{RF} , frequency-modulating the excitation at f_{FM} and with a $\pm \Delta f_{FM}$ deviation. The same generator additionally isolates the modulation component P_{FM} , for a successive synchronous lock-in detection. In liquid He, the excitation system, consisting of the Cu GCPW electromagnetically coupled to the S-SRRs, is encapsulated inside a cylindrical enclosure made of CRYOPHY®. At room temperature, the microwave signal is amplified (B. *Mini-Circuits ZRL-1150LN*) and converted into a DC value proportional to its amplitude by means of a microwave diode detector (C. *Macom 2086-6000-13*). The signal is then split, with the DC component further amplified (D. *EG&G Princeton Applied Research Model 5113*), with a low-pass filter set to 30 kHz, and the AC one detected by means of a lock-in amplifier (E. *EG&G Instruments Model 7265*), with a 100 ms time constant, whose reference is externally provided by the same exciting microwave generator. Finally, both DC, in-phase (X) and quadrature (Y) components are simultaneously acquired by a data acquisition (DAQ) board with a 100 ms integration time (F. *PCI-6052E*).

The following sub-sections are intended for reporting the experimental procedures adopted to identify the values of excitation power P_{RF} , modulation frequency f_{FM} and amplitude Δf_{FM} . All the following preliminary experiments are carried out only on the 147 nm thick S-SRR.

S5.1 Excitation power P_{RF} (Δf_{FM} , f_{FM} fixed)

The excitation microwave power P_{RF} is determined along this section, by making a power sweep from -30 dBm to -20 dBm and keeping the modulation frequency and amplitude fixed (*i.e.* $f_{FM} = 11$ kHz and $\Delta f_{FM} = \pm 5$ kHz). As expected for an increase of the excitation intensity, a larger dV/df curve slope is observed, increasing with the power, for both the DC and X signal components [see Fig. S7(a-d)], with maximum values around 0.14 V/MHz and 0.04 V/MHz

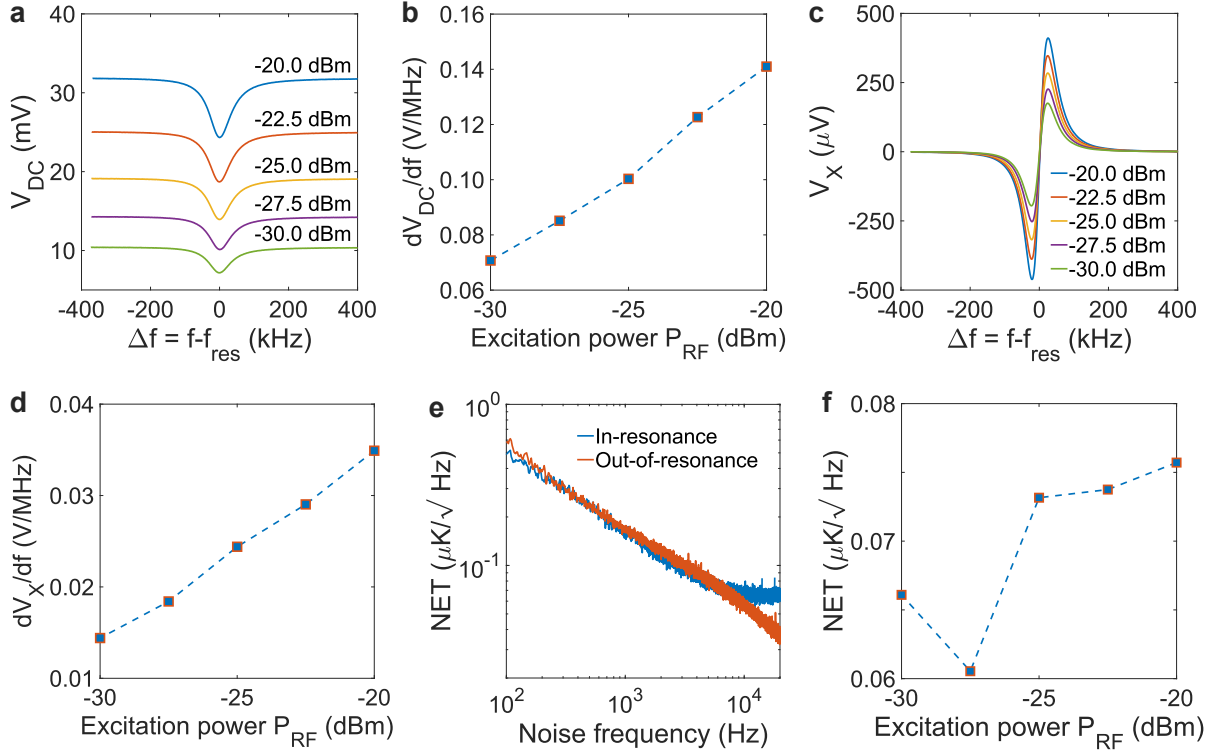


Figure S7: Determination of the excitation power P_{RF} . a) DC skewed-Lorentzian resonance curve ($f_{res} = 1.1391$ GHz and $Q_L = 1.41 \times 10^4$) under different input powers. b) Maximum DC signal slope versus excitation power. c) X signal under different RF input powers. d) Maximum X signal slope versus excitation power. e) Frequency spectrum of the noise equivalent temperature for the DC signal at -27.5 dBm. The blue curve represents the NET extracted for the signal maximum slope condition, while the orange one stands for the out-of-resonance case. f) NET evaluated at 10 kHz, under different RF excitation powers.

respectively. Moreover, the DC NET for all the power values under test is also extracted, for the signal maximum slope case (*i.e.* $\Delta f = -18$ kHz), as well as for an out-of-resonance condition (*i.e.* $\Delta f = 400$ kHz). It is interesting to notice that the coincidence of the two curves, showing a $1/f$ behavior up to a 10 kHz corner frequency for the in-resonance signal, suggests that the noise originates from the electronic instrumentation involved [see Fig. S7(e)]. This result justifies the choice of FM techniques, in order to transfer low-frequency signals to frequencies above the corner, without any additional transfer of instrumentation noise. Finally, as reported in Fig. S7(f), the fact that no significant difference is recorded for the minimum temperature resolutions (around $0.07 \mu\text{K}/\text{Hz}^{1/2}$), in this specific power range, motivates the choice of a -20 dBm microwave excitation for further cryogenic tests, in order to take advantage of the higher temperature responsivity of the DC and X signals. Larger excitation powers are not considered in this work, because of possible self-heating and peak distortions due to non-linear effects.

S5.2 Modulation amplitude Δf_{FM} (P_{RF} , f_{FM} fixed)

The modulation amplitude Δf_{FM} is determined along this section, by making a sweep from ± 5 kHz to ± 40 kHz and keeping the microwave excitation power and the modulation frequency fixed (*i.e.* $P_{RF} = -20$ dBm and $f_{FM} = 11$ kHz). In Fig. S8(a-b), both the DC and X signals versus frequency, for different FM amplitudes, are presented. In particular, the slope of the DC component is showing significant distortions, turning away from linearity, starting from ± 20 kHz [see Fig. S8(c)], due to the frequency deviation starting to be comparable with the FWHM on the skewed-Lorentzian curve of 80 kHz. Moreover, preliminary estimations of the NET , by exciting the S-SRR with higher Δf_{FM} , have not shown any reduction of the temperature resolution. As illustrated in Sec. S6, we observe that the major sources of noise are related to the physical environment (*i.e.* He temperature, dewar pressure, magnetic field, etc...). In such a perspective, a larger Δf_{FM} results in the same amplification factor for both signal and environmental fluctuations, making no significant improvement in the estimation of the NET . An FM deviation equal to ± 5 kHz is, therefore, selected for performing further cryogenic tests.

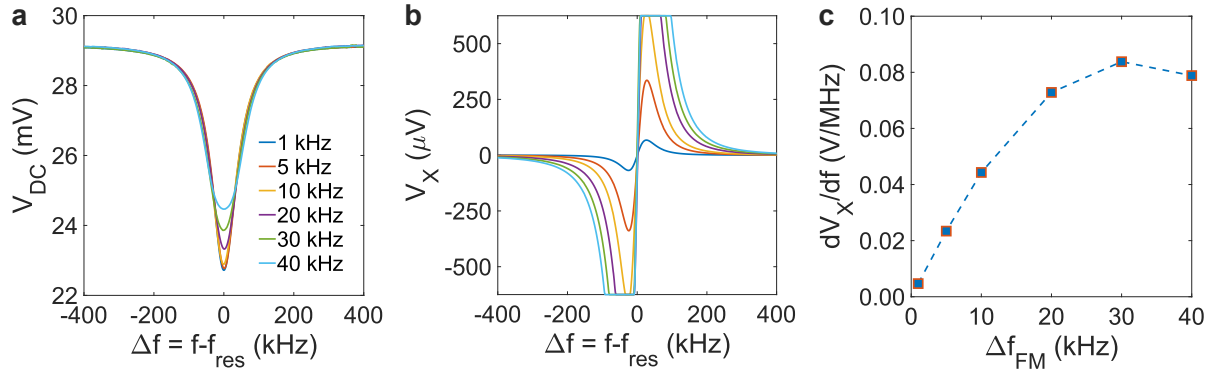


Figure S8: Determination of the modulation amplitude Δf_{FM} . a) DC skewed-Lorentzian resonance curve ($f_{res} = 1.1391$ GHz and $Q_L = 1.41 \times 10^4$) under different FM amplitudes. b) X signal under different FM amplitudes: the color legend is the same as the one reported for the DC signal graph. c) Maximum X signal slope (in-resonance) versus FM amplitude.

S5.3 Modulation frequency f_{FM} (P_{RF} , Δf_{FM} fixed)

The modulation frequency f_{FM} is determined along this section, by extracting the X-signal *NET* for three different FMs: around 1 kHz (well below the $1/f$ -noise corner frequency), 11 kHz (slightly above the corner frequency) and 41 kHz (well above the corner frequency). In this case, the microwave excitation power and the modulation amplitude are kept fixed (*i.e.* $P_{RF} = -20$ dBm and $\Delta f_{FM} = \pm 5$ kHz). Fig. S9(a) reports the typical response of the DC and X signals, for $f_{FM} = 11$ kHz, with respective maximum slopes dV/df of 0.10 V/MHz and 0.02 V/MHz. The DC *NET* is presented in Fig. S9(b), being acquired with a 1 s integration time, a 200 kHz sampling rate and a low-pass filter set to 30 kHz, to avoid possible aliasing. Since the system exhibits a $1/f$ behavior below a corner frequency around 10 kHz, an FM value situated above such a corner must be selected, in order to properly apply lock-in detection techniques to reduce the instrumentation noise. A modulation frequency equal to 11 kHz is, therefore, selected for performing further cryogenic tests, as values below the corner condition significantly deteriorate the temperature resolution [see Fig. S9(c)].

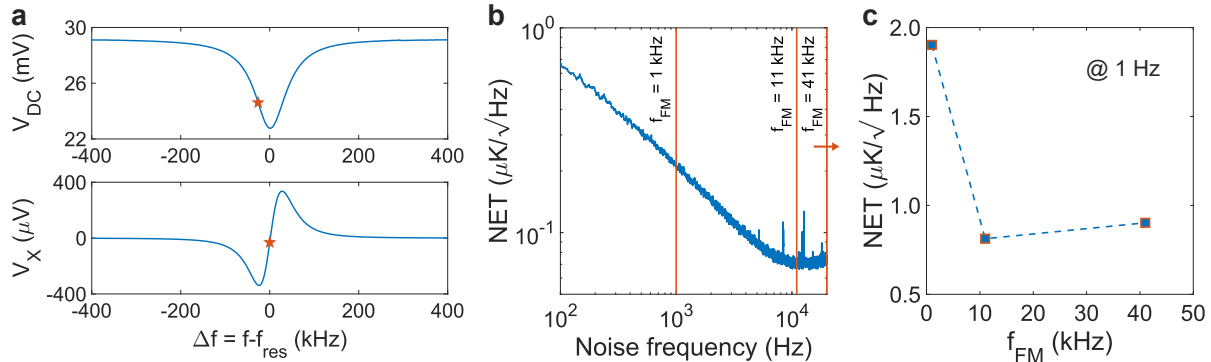


Figure S9: Determination of the modulation frequency f_{FM} . a) DC (top) and X (bottom) resonance signals ($f_{res} = 1.1391$ GHz and $Q_L = 1.41 \times 10^4$). The single orange points indicate the condition of maximum slopes for both curves, where time scans get carried out to extract the respective low-frequency NSDs. b) Noise spectrum of the DC equivalent temperature, extracted while time-monitoring the signal in resonance (*i.e.* for $\Delta f = -18$ kHz). The orange vertical lines represent the modulation frequencies selected to perform the X-signal lock-in monitoring. c) X signal *NET*, evaluated at 1 Hz, for different choices of the modulation frequency.

S6 Simultaneous temperature monitoring in liquid He

The aim of this section is to describe the experimental setup exploited to perform the simultaneous characterization of two-out-of-three resonators at 4.2 K, as well as to provide the results concerning the time-domain temperature monitoring of the LHe bath.

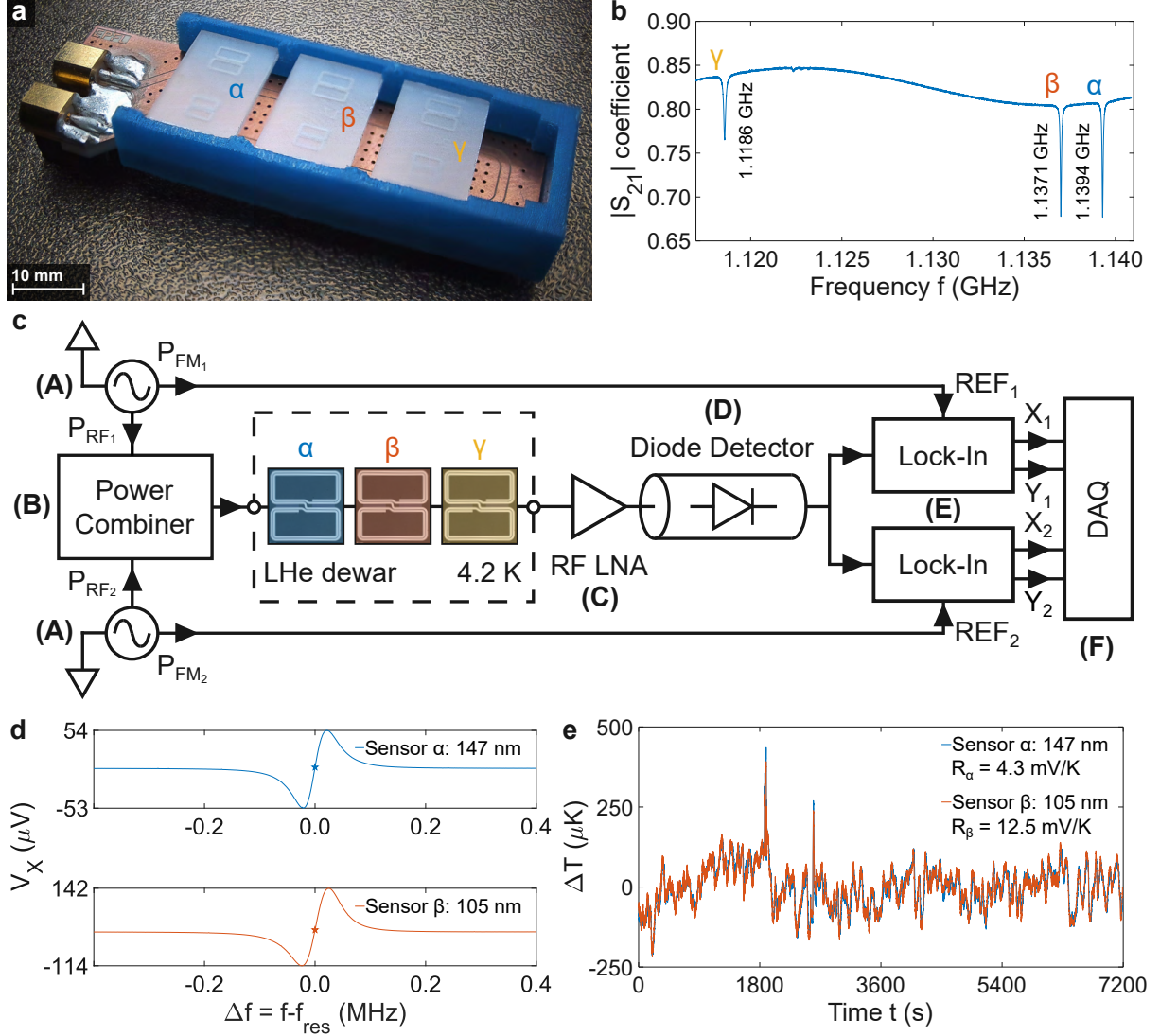


Figure S10: Two resonators simultaneous temperature monitoring at 4.2 K in a LHe dewar. a) PCB exploited to excite multiple resonators, by means of a single Cu GCPW. b) S_{21} transmission parameter frequency scan, in liquid He at 4.2 K. From left to right, it is possible to clearly distinguish the presence of the three different resonance peaks, respectively related to the 57 nm, 105 nm and 147 nm thick S-SRRs. c) Experimental setup used to simultaneously excite two-out-of-three S-SRRs, by means of two microwave signals frequency-modulated at two different values. d) Simultaneous frequency scan of the X signals for the 147 nm and 105 nm thick devices (Sensor α : $f_{res} = 1.1394$ GHz and $Q_L = 1.67 \times 10^4$; Sensor β : $f_{res} = 1.1371$ GHz and $Q_L = 1.61 \times 10^4$). The single points represent the zero-crossing resonance frequency, showing the maximum slope values. e) 2 h time evolution of the two X signals, simultaneously exciting the two S-SRRs at their corresponding resonance frequency.

Fig. S10(a) shows the Cu PCB used to excite three different S-SRRs in parallel, resonating around 1.1 GHz. The 3D-printed PLA support is re-designed in order to host three chips (*i.e.* the 147 nm, 105 nm and 57 nm thin-films), 2.5 mm far from the GCPW and approximatively spaced by 11 mm. The exact value of each resonance frequency, at 4.2 K, is preliminarily determined by performing a frequency scan with a VNA (*PicoVNA 108*), delivering an excitation power of -20 dBm. Each of the peaks is well separated from the others by several MHz, allowing to unambiguously identify a different excitation frequency for each of them [see Fig. S10(b)].

Once having located the different resonances, we excite two-out-of-three resonators for monitoring the temperature fluctuations of liquid He, by means of two distinct lock-in detections. In Fig. S10(c) we report a schematic of the instrumentation setup exploited to excite both the 147 nm and 105 nm thick S-SRRs. Two different signal generators (A. *Stanford Research SG384*) are exploited to provide distinct -20 dBm microwave powers, each of them respectively

frequency-modulated at 11 kHz and 18 kHz, with an amplitude of ± 5 kHz. The power combination (**B. Mini-Circuits ZFM-2000+**) of these signals is then used to excite the GCPW, coupled to the resonators, in liquid He. After amplification and DC conversion at room temperature, by means of a low-noise amplifier (**C. Mini-Circuits ZRL-1150LN**) and a diode detector (**D. Macom 2086-6000-13**), the AC component of the transmitted signal is detected by two different lock-in amplifiers (**E. EG&G Instruments Model 7265**), with a 100 ms time constant, each of them referenced to the corresponding modulation frequency, in order to decouple the response of the individual resonators. Finally, the four signals, X and Y outputs for both resonators, are acquired by a DAQ with a 100 ms integration time (**F. PCI-6052E**). The X-signals for both resonators are plotted in [Fig. S10\(d\)](#), showing a maximum in-resonance slope of about 4.2 mV/MHz for sensor α and 8.9 mV/MHz for sensor β . A 2 h time scan is then carried out in parallel on the two different devices [see [Fig. S10\(e\)](#)], at their corresponding resonance frequencies. The measured voltages are converted in temperature variations by normalizing each dataset to the corresponding temperature responsivity (*i.e.* $R_\alpha(4.2\text{ K}) = 4.3\text{ mV/K}$ and $R_\beta(4.2\text{ K}) = 12.5\text{ mV/K}$ respectively), showing temperature fluctuations in the order of $100\text{ }\mu\text{K}$. The coincidence of the two time scans suggests the measured low-frequency fluctuations to originate from temperature-related environmental phenomena, rather than from the noise associated to each resonator.

S7 Low-frequency temperature fluctuations in liquid He

In this last section, we discuss about the experiment carried out to further investigate the origin of the low-frequency temperature fluctuations. As reported in the main text, the temperature of the LHe dewar is now simultaneously monitored by exploiting two devices relying on different sensing principles: the 147 nm thick $L_K(T)$ -based S-SRR and a commercial RuO_2 thermistor (*i.e.* RO-600 by *Scientific Instruments, Inc.*, showing a $1.36\text{ k}\Omega$ resistance and a temperature sensitivity of $-86\text{ }\mu\text{K}/\text{K}$ at 4.2 K)⁷.

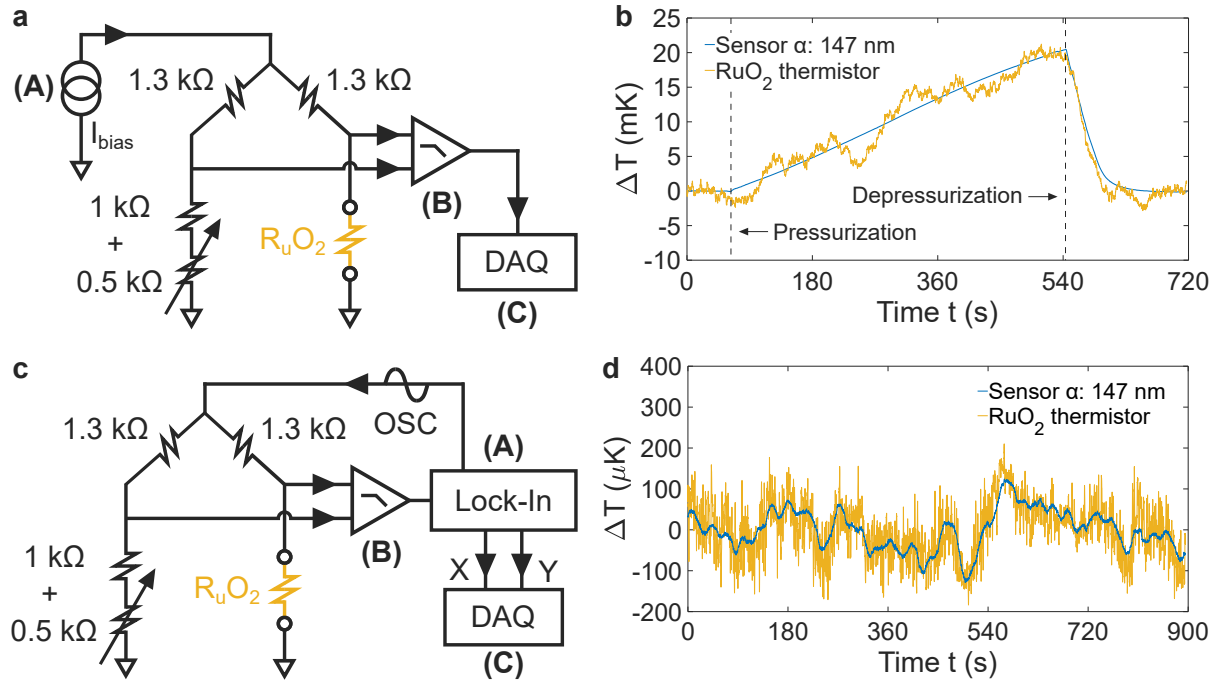


Figure S11: Parallel temperature monitoring of the LHe bath at 4.2 K, exploiting the 147 nm thick S-SRR and a commercial RuO_2 thermistor. a) DC Wheatstone bridge experimental setup used to bias the thermistor. b) Comparison of the temperature reading of the S-SRR versus the RuO_2 one, when performing a pressurization/depressurization of the LHe dewar. c) AC Wheatstone bridge experimental setup used to bias the thermistor, when implementing a lock-in detection scheme. d) Simultaneous temperature monitoring of the low-frequency fluctuations, performed exploiting two lock-in detections on both the S-SRR sensor and the RuO_2 thermistor.

The excitation of the S-SRR is provided by the same instrumentation setup reported in [Fig. S6](#), by acquiring the demodulated X-signal at the output of a lock-in amplifier. The excitation parameters are the same optimal ones identified in [Sec. S5](#) (*i.e.* $P_{RF} = -20\text{ dBm}$, $f_{FM} = 11\text{ kHz}$ and $\Delta f_{FM} = \pm 5\text{ kHz}$). As depicted in [Fig. S11\(a\)](#), the RuO_2 thermistor is excited by means of a balanced Wheatstone bridge, kept at room temperature and biased through a sourcemeter (A).

Keithley 2400) delivering a $20\ \mu\text{A}$ DC current. A $500\ \Omega$ potentiometer, in series to a $1\ \text{k}\Omega$ resistor, is placed on the branch opposite to the temperature-sensitive element, in order to accurately cancel out the differential voltage reading and balance the bridge. The voltage difference between the two branches is, then, amplified (**B. EG&G Princeton Applied Research Model 5113**), low-pass filtered, with a 3 Hz bandwidth, and finally acquired by a DAQ board with a 100 ms integration time (**C. PCI-6052E**). The RuO_2 thermometer is connected, in a 4-wires configuration, to the DC pads of the Cu PCB and placed at a distance of about 1 cm far from the S-SRR.

A preliminary experiment is carried out in order to check the correct functioning of the sensors. A relatively large pressure-induced temperature perturbation of about 20 mK is generated by closing and opening the valve connecting the LHe dewar to a gas recovery line. In [Fig. S11\(b\)](#) we present the monitoring of the temperature along this test. The temperature of the LHe bath increases linearly upon closing the valve, because of the increase of the internal vapor pressure. When opening the valve, the systems converges back to the initial situation through an exponential decay. Moreover, we also record an almost 20 mbar increase in the internal pressure of the dewar, by means of a barometer placed on the head of the dewar, which should ideally correspond to a temperature increase of about 20 mK for boiling liquid He at 4.2 K⁸. The coincidence of the two responses, upon voltage-to-temperature conversion, as well as the value of the overall temperature shift, is an indicator of the reliability of the temperature reading through both sensors. The noise level of the thermistor (about 2 mK) turns out to be almost 400 times higher than the one associated to the resonator (about $5\ \mu\text{K}$). Such a relatively poor temperature resolution, for the DC-biased thermistor, would theoretically prevent the ultimate detection of the low-frequency temperature fluctuations, in the order of $100\ \mu\text{K}$.

As an attempt to further reduce the noise associated to the RuO_2 , a lock-in detection scheme is implemented also on the temperature reading of the thermistor [see [Fig. S11\(c\)](#)]. The oscillator output of a lock-in amplifier (**A. Stanford Research SR830**) is now exploited to bias the bridge with a $26\ \text{mV}_{\text{RMS}}$ voltage, corresponding to a $10\ \mu\text{A}_{\text{RMS}}$ current flowing across the sensing branch. The biasing voltage is oscillating at 17 kHz, which is also exploited as lock-in internal modulation reference. The differential voltage reading is amplified (**B. EG&G Princeton Applied Research Model 5113**), filtered (with a band-pass between 1 kHz and 100 kHz) and acquired, as X-signal output of the lock-in amplifier, with a 100 ms time constant, by a DAQ board with a 100 ms integration time (**C. PCI-6052E**). A 2 h scan is performed, on both the X outputs related to the S-SRR and the RuO_2 sensor. In [Fig. S11\(d\)](#) we report a 15 min time lapse of the two temperature readings. Low-frequency fluctuations in the order of $100\ \mu\text{K}$ are clearly distinguishable on both signals. The coincidence of the responses for the two sensors, each of them exploiting a different physical phenomenon to probe temperature, confirms the origin of such fluctuations to be related to environmental effects inducing sub-mK temperature variations in the LHe bath.

References

- [1] S. Mohan, M. del Mar Hershenon, S. Boyd, and T. Lee, [IEEE J. Solid-State Circuits](#) **34**, 1419 (1999).
- [2] H. A. Aebischer, [Adv. Electromagn.](#) **9**, 1 (2020).
- [3] J. Gao, *The physics of superconducting microwave resonators*, [PhD thesis](#), California Institute of Technology (2008).
- [4] M. Tinkham, *Introduction to superconductivity*, 2nd ed. (Dover, Mineola, N.Y., 2004).
- [5] A. J. Annunziata, D. F. Santavica, L. Frunzio, G. Catelani, M. J. Rooks, A. Frydman, and D. E. Prober, [Nanotechnol.](#) **21**, 445202 (2010).
- [6] L. Nulens, N. Lejeune, J. Caeyers, S. Marinković, I. Cools, H. Dausy, S. Basov, B. Raes, M. J. Van Bael, A. Geresdi, A. V. Silhanek, and J. Van de Vondel, [Commun. Phys.](#) **6**, 267 (2023).
- [7] G. G. Ihas, L. Frederick, and J. P. McFarland, [J. Low Temp. Phys.](#) **113**, 63 (1998).
- [8] R. J. Donnelly and C. F. Barenghi, [J. Phys. Chem. Ref. Data](#) **27**, 1217 (1998).